Experimental validation of flexible multibody dynamics beam formulations*

Olivier A. Bauchau*, Shilei Han*, Aki Mikkola†,
Marko K. Matikainen†, and Peter Gruber‡
*University of Michigan-Shanghai Jiao Tong University Joint Institute
800 Dong Chuan Road, Shanghai, 200240, China
†Department of Mechanical Engineering
Lappeenranta University of Technology, 53851 Lappeenranta, Finland
‡Austrian Center of Competence in Mechatronics GmbH
4040 Linz, Austria

July 12, 2015

Abstract

In this paper, the accuracies of the geometrically exact beam and absolute nodal coordinate formulations are studied by comparing their predictions against an experimental data set referred to as the "Princeton beam experiment." The experiment deals with a cantilevered beam experiencing coupled flap, lag, and twist deformations. In the absolute nodal coordinate formulation, two different beam elements are used. The first is based on a shear deformable approach in which the element kinematics is described using two nodes. The second is based on a recently proposed approach featuring three nodes. The numerical results for the geometrically exact beam formulation and the recently proposed three-node absolute nodal coordinate formulation agree well with the experimental data. The two-node beam element predictions are similar to those of linear beam theory. This study suggests that a careful and thorough evaluation of beam elements must be carried out to assess their ability to deal with the three-dimensional deformations typically found in flexible multibody systems.

1 Introduction

The simulation of helicopter rotor blade dynamics is a difficult problem because nonlinearities affect the response of the system. In 1958, Houbolt and Brooks [1] derived the differential equations of motion for the combined flapwise bending, chordwise bending, and torsion of twisted nonuniform rotor blades. Their approach was based on a modal representation of the blade's response and the equations of motion were developed in a frame of reference that rotated with the rotor. Due to poor correlation with flight test measurements, the accuracy of this formulation was questioned.

In 1974, Hodges and Dowell [2] developed a more accurate set of equations for the same problem: nonlinear terms were handled carefully, although terms of order higher than second were neglected. To assess the accuracy of these equations, Dowell and Traybar [3, 4] carried out an experimental study of the nonlinear stiffness of a rotor blade undergoing flap, lag, and twist deformations, often

Multibody System Dynamics, **34**(4): pp 373-389, 2015

referred to as the "Princeton beam experiment." Although the correlation of the Hodges-Dowell predictions with this data set was not very good, the analysis was deemed sufficiently accurate for hingeless helicopter rotor blade dynamics and aeroelasticity, because they involve moderately large deformations only.

The Princeton beam experiment presents the static deflections of a simple cantilevered beam under various loading conditions. Yet, this static experiment was used for the validation of beam models developed for rotor dynamics. In this paper, a similar approach is followed: the same static experimental data will be used for the validation of flexible multibody dynamics beam formulations.

The dynamic response of bearingless rotor blades is affected more significantly by nonlinear behavior than that of articulated blades. In the late 1970s, it was recognized that bearingless rotor problems demanded a more accurate theory, and many researchers started focusing on geometrically exact beam theories. The kinematics of the geometrically exact beam formulation was first presented by Simo *et al.* [5, 6], but similar developments were proposed by Borri and Merlini [7], Danielson and Hodges [8, 9], or Bauchau and Hong [10, 11, 12]. The Princeton beam experiment was used as a benchmark to assess the accuracy of these formulations.

The previous paragraphs have summarized in a succinct manner some the milestones in the development of accurate equations for the modeling of helicopter rotor blades. Similar steps can be found in the development of simulation tools for flexible multibody dynamics, which originally focused on simple tree-like topologies composed of rigid bodies. As the need to model flexibility arose, the floating frame of reference formulation [13, 14, 15] was developed; this solution strategy is akin to the approach of Houbolt and Brooks for helicopter rotors.

Because floating frame of reference formulations were found to yield inaccurate results when elastic deformations become large, the multibody dynamics community began to turn its attention to geometrically exact beam formulations (GEBF). other approaches have been proposed for the analysis of beams undergoing large motion, the GEBF is probably the best established formulation. The authors cited above have proposed different numerical implementations of the theory, but all solve the geometrically exact beam equations. In recent years, the absolute nodal coordinate formulation (ANCF) has been developed and has received considerable attention for the modeling of flexible multibody systems. Clearly, the developments in the multibody dynamics community parallel those of the rotorcraft community. The GEBF and ANCF involve fewer assumptions than the floating frame of reference approach, but little effort has been devoted to the systematic comparison of these two approaches.

Romero [16] has presented a comparison of both qualitative and quantitative aspects of the two approaches. He concluded that the ANCF is more straightforward, while GEBF involves thorny issues, such as the treatment of finite rotations. Unfortunately, the ANCF suffers from a number of locking mechanisms that must be eliminated to obtain accurate results. As pointed out by Gerstmayr *et al.* [17], this can be accomplished in a number of ways, but the proposed techniques complicate the description of elastic forces, leading to more arduous implementations and moving away from the simplicity of the initial implementation. In some of the examples treated by Romero, the ANCF and GEBF did not converge to the same solution. In all cases, the computational efficiency of the GEBF was found to be far superior to that of the ANCF.

Bauchau *et al.* [18] further compared the GEBF and ANCF to identify the causes of their differing computational efficiencies for the two-dimensional beam case. First, they performed a kinematic solution, in which the exact nodal displacements were prescribed and the interpolated displacement and strain fields were compared for the two methods. The accuracies of the interpolated strain fields were found to differ markedly: the predictions of the GEBF were far more accurate than those of the ANCF. They attributed this phenomenon to the fact that the curvature field is obtained as a second derivative of the displacement in the ANCF, but as a first derivative only for the GEBF. Next, they carried out a static solution to determine the solution of the problem. For the GEBF, the predictions of the static solution are far more accurate than those obtained from the kinematic

solution; in contrast, the same order of accuracy was obtained for the two solution procedures when using ANCF. In all cases, they reported that the predictions of the GEBF are more accurate than those of the ANCF.

The comparative studies of Romero and Bauchau *et al.* were of a purely numerical nature, and hence, validation against experimental data is needed to come to a definite conclusion. Because the Princeton beam experiment focused on applications to helicopter rotor blades, this data set has received little attention outside the rotorcraft community. The goal of this paper is to validate several beam theories used in flexible multibody dynamics simulations against the Princeton beam experiment.

2 Formulation of beam elements

In Euler-Bernoulli beam and Kirchhoff plate formulations, transverse shear strains are assumed to vanish and hence, rotation of the cross-sectional plane and of the normal material line, respectively, are obtained from derivatives of the displacement field, and curvatures are expressed in terms second derivatives of the same field [19]. In contrast, shear deformable beams and plates, often called Timoshenko beams [20, 21] and Reissner-Mindlin plates [22, 23], respectively, are Cosserat solids: the kinematics of these structural components are described in terms of two independent fields, a displacement field and a rotation field. Reissner investigated beam theory for large strains [24] and large displacements of spatially curved members [25, 26].

In two- and three-dimensional elasticity, the rotation field is not independent of the displacement field. Indeed, the polar decomposition theorem can be used to decompose the deformation gradient tensor into a stretch tensor and an orthogonal rotation tensor [27]. Because this decomposition is unique, the deformation gradient tensor, a function of the displacement field only, defines the rotation field unambiguously. This contrasts with Cosserat solids for which the displacement and rotation fields are independent.

A beam is defined as a structure having one of its dimensions much larger than the other two, as depicted in fig. 1. The axis, or reference line, of the beam is defined along that longer dimension and its cross-section is normal to this axis. The cross-section's geometric and physical properties are assumed to vary smoothly along the beam's span.

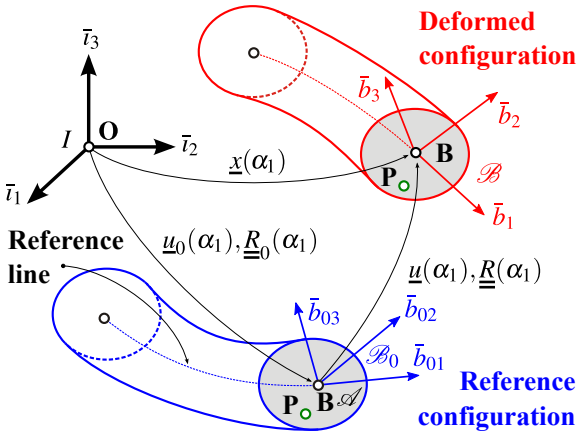

Figure 1: Curved beam in the reference and deformed configurations.

Figure 1 depicts an initially curved and twisted beam of length L, with a cross-section of arbitrary shape and area $\mathcal{A}$. The volume of the beam is generated by sliding the cross-section along the reference line of the beam, which is defined by an arbitrary curve in space. Curvilinear coordinate α_1 defines the intrinsic parameterization of this curve, *i.e.*, it measures length along the beam's

reference line. Point **B** is located at the intersection of the reference line with the plane of the cross-section.

2.1 Kinematics of the problem

In the reference configuration, an orthonormal basis, $\mathcal{B}_0(\alpha_1) = (\bar{b}_{01}, \bar{b}_{02}, \bar{b}_{03})$, is defined at point **B**. Vector $\bar{b}_{01}$ is the unit tangent vector to the reference curve at that point, and unit vectors $\bar{b}_{02}$ and $\bar{b}_{03}$ define the plane to the cross-section. An inertial reference frame, $\mathcal{F}_I = [\mathbf{O}, \mathcal{I} = (\bar{\imath}_1, \bar{\imath}_2, \bar{\imath}_3)]$, is defined, and the components of the rotation tensor that brings basis $\mathcal{I}$ to $\mathcal{B}_0$, resolved in basis $\mathcal{I}$, are denoted $\underline{\underline{R}}_0(\alpha_1)$.

The position vector of point **B** along the beam's reference line is denoted $\underline{u}_0(\alpha_1)$. The position vector of material point **P** of the beam then becomes $\underline{x}(\alpha_1, \alpha_2, \alpha_3) = \underline{u}_0(\alpha_1) + \alpha_2\, \bar{b}_{02} + \alpha_3\, \bar{b}_{03}$, where α_2 and α_3 are the material coordinates along unit vectors $\bar{b}_{02}$ and $\bar{b}_{03}$, respectively. Coordinates α_1, α_2, and α_3 form a natural choice of coordinates to represent the configuration of the beam.

In the deformed configuration, all the material points located on a cross-section of the beam move to new positions. This motion is decomposed into two parts, a rigid-body motion and a warping displacement field. The rigid-body motion consists of a translation of the cross-section, characterized by displacement vector $\underline{u}(\alpha_1)$ of reference point **B**, and of a rotation of the cross-section, which brings basis $\mathcal{B}_0$ to $\mathcal{B}(\alpha_1) = (\bar{b}_1, \bar{b}_2, \bar{b}_3)$, see fig. 1. The components of the position vector of point **B** in the deformed configuration is denoted $\underline{x}(\alpha_1)$ and the components of the rotation tensor that brings basis $\mathcal{B}_0$ to $\mathcal{B}$ are denoted $\underline{\underline{R}}(\alpha_1)$; all tensor components are resolved in basis $\mathcal{I}$.

For shear deformable beams, the deformation is characterized by six sectional strains: the axial strain, the two transverse shear strains, the twist rate, and the two bending curvatures. Of course, for Euler-Bernoulli beams, the two transverse shear strains are assumed to vanish.

2.2 Geometrically exact beam formulation

In this section, the *geometrically exact beam theory* will be summarized. The kinematic description of the problem developed in section 2.1 accounts for arbitrarily large displacements and rotation, hence the term "geometrically exact," although the strain components are assumed to remain small.

2.2.1 Definition of strain measures

The sectional strain measures for beams are defined as

$$\underline{\mathcal{E}} = \begin{Bmatrix} \underline{\Gamma} \\ \underline{\Lambda} \end{Bmatrix} = \begin{Bmatrix} \underline{x}_0' + \underline{u}' - (\underline{\underline{R}}\,\underline{\underline{R}}_0)\ \bar{\imath}_1 \\ \text{axial}(\underline{\underline{R}}'\,\underline{\underline{R}}^T) \end{Bmatrix}, \tag{1}$$

The sectional strain vector is defined as $\underline{\Gamma}^T = \{\Gamma_{11}, \Gamma_{12}, \Gamma_{13}\}$, where Γ_{11} is the sectional axial strain, and Γ_{12} and Γ_{13} the two components of transverse shearing strains. The curvature vector is defined as $\underline{\Lambda}^T = \{\Lambda_1, \Lambda_2, \Lambda_3\}$, where Λ_1 is the sectional twist rate, and Λ_2 and Λ_3 the two bending curvatures. Notation $(\cdot)'$ indicates a derivative with respect to α_1. The strain components resolved in the convected material basis, $\mathcal{B}$, are denoted $\underline{\Gamma}^* = (\underline{\underline{R}}\,\underline{\underline{R}}_0)^T\underline{\Gamma}$. The curvature components resolved in the same material basis are denoted $\underline{\Lambda}^* = (\underline{\underline{R}}\,\underline{\underline{R}}_0)^T\underline{\Lambda}$. Notation $(\cdot)^*$ indicates the components of vectors and tensors resolved in the material basis.

By definition, a rigid-body motion is a motion that generates no strains. This implies that the following rigid-body motion, $\underline{u}(\alpha_1) = \underline{u}^R + (\underline{\underline{R}}^R - \underline{\underline{I}})\underline{x}_0(\alpha_1)$, $\underline{\underline{R}}(\alpha_1) = \underline{\underline{R}}^R$, consisting of a translation, $\underline{u}^R$, and a rotation about the origin characterized by a rotation tensor, $\underline{\underline{R}}^R$, should not strain the beam. It can be verified readily with the help of eqs. (1) that such rigid-body motion results in $\underline{\Gamma} = 0$ and $\underline{\Lambda} = 0$, as expected.

2.2.2 Equations of motion

The derivation of the equations of motion for geometrically exact beams can be found in textbooks such as those of Hodges [28] or Bauchau [29] and will not be repeated here. The governing equations are

$$\dot{\underline{h}} - \underline{N}' = \underline{f}, \tag{2a}$$

$$\dot{\underline{g}} + \dot{\tilde{u}}\ \underline{h} - \underline{M}' - (\tilde{x}_0' + \tilde{u}')\underline{N} = \underline{m}. \tag{2b}$$

The externally applied forces and moments per unit span of the beam are denoted $\underline{f}$ and $\underline{m}$, respectively. The beam's sectional forces and moments are denoted $\underline{N}$ and $\underline{M}$, respectively. Finally, the components of the sectional linear and angular momenta are denoted $\underline{h}$ and $\underline{g}$, respectively. Notation $(\cdot)^{\cdot}$ indicates a derivative with respect to time. The governing equations of motion (2) express the dynamic equilibrium conditions of the beam at each instant. To form a complete set, constitutive laws for both sectional forces and momenta are required.

The sectional forces and moments are related to the sectional strain and curvature components through the following constitutive laws

$$\begin{Bmatrix} \underline{N}^* \\ \underline{M}^* \end{Bmatrix} = \underline{\underline{\mathcal{D}}}^* \begin{Bmatrix} \underline{\Gamma}^* \\ \underline{\Lambda}^* \end{Bmatrix}, \tag{3}$$

where $\underline{N}^*$ and $\underline{M}^*$ are the beam's sectional forces and moments, respectively, and $\underline{\Gamma}^*$ and $\underline{\Lambda}^*$ the sectional strains and curvatures, respectively, resolved in the material basis. In eq. (3), $\underline{\underline{\mathcal{D}}}^*$ is the beam's 6×6 sectional stiffness matrix. This matrix is a byproduct of a two-dimensional finite element analysis over the beam's cross-section, as discussed in refs. [30, 28, 31]. For homogeneous sections of simple geometry, exact or approximate analytical expressions are available for the stiffness matrix. The strain energy stored in the beam is then

$$A = \frac{1}{2}\int_0^L \underline{\mathcal{E}}^{*T}\underline{\underline{\mathcal{D}}}^*\underline{\mathcal{E}}^*\ \mathrm{d}\alpha_1. \tag{4}$$

The linear and angular momenta are related to the sectional linear and angular velocities through the following constitutive laws

$$\begin{Bmatrix} \underline{h}^* \\ \underline{g}^* \end{Bmatrix} = \begin{bmatrix} m\underline{\underline{I}} & m\tilde{\eta}^{*T} \\ m\tilde{\eta}^* & \underline{\underline{\varrho}}^* \end{bmatrix} \begin{Bmatrix} (\underline{\underline{R}}\,\underline{\underline{R}}_0)^T\dot{\underline{u}} \\ (\underline{\underline{R}}\,\underline{\underline{R}}_0)^T\underline{\omega} \end{Bmatrix}, \tag{5}$$

where $\underline{h}^*$ and $\underline{g}^*$ the components of the sectional linear and angular momenta resolved in the material system, respectively, and $\dot{\underline{u}}$ and $\underline{\omega}$ the inertial linear and angular velocities of the cross-section, respectively. The components of linear and angular momenta resolved in the material basis are related to their counterparts in the inertial system as $\underline{h} = (\underline{\underline{R}}\,\underline{\underline{R}}_0)\underline{h}^*$ and $\underline{g} = (\underline{\underline{R}}\,\underline{\underline{R}}_0)\underline{g}^*$. In eq. (5), the following sectional mass constants were defined

$$m = \int_{\mathcal{A}} \rho\ \mathrm{d}\mathcal{A},\ \underline{\eta}^* = \frac{1}{m}\int_{\mathcal{A}} \rho\,\underline{s}^*\ \mathrm{d}\mathcal{A},\ \underline{\underline{\varrho}}^* = \int_{\mathcal{A}} \rho\tilde{s}^*\tilde{s}^{*T}\ \mathrm{d}\mathcal{A}, \tag{6}$$

where m is the mass of the beam per unit span, $\underline{\eta}^*$ the components of the position vector of the sectional center of mass with respect to point $\mathbf{B}$, see fig. 1, and $\underline{\underline{\varrho}}^*$ the components of the sectional tensor of inertia per unit span, all resolved in the material basis.

2.3 Absolute nodal coordinate formulation

According to Gerstmayr *et al.* [17], beam elements based on the ANCF fall into two groups. The first group is based on Euler-Bernoulli kinematics, *i.e.*, transverse shear deformations are assumed to vanish. These elements, often referred to as "gradient deficient elements," are approximated as line elements and use position coordinates and longitudinal slopes variables only. The second group is based on Timoshenko kinematics, *i.e.*, transverse shear deformations do not vanish. In addition to the variables found in their gradient deficient counterparts, these elements, referred to as "fully parameterized elements," also feature variables that describe transverse slope vectors, thereby allowing the description of transverse shear and cross-sectional deformations.

In this study, two- and three-node shear deformable beam elements [32, 33] are used to assess the ANCF. The two-node elements introduced by Dufva *et al.* [32] have longitudinal and transverse slope vectors, while the recently introduced three-node elements [33] have transverse slope vectors only. Both elements are based on a structural mechanics approach, but use different strain energy definitions. Furthermore, both elements use a different interpolation order.

The fully parameterized, two-node beam elements first introduced by Shabana and Yakoub [34] used cubic interpolation of displacements along the beam's span and linear interpolation over its cross-section. This element converged slowly due to transverse shear locking: indeed, the transverse and longitudinal slope vectors were approximated using different polynomial orders. This mismatch of interpolation orders led to shear locking, which can be eliminated using a mixed interpolation approach, as presented Dufva *et al.* [32].

Nachbagauer *et al.* [33] proposed three-node beam elements featuring quadratic interpolation of displacements along the beam's span and linear interpolation over its cross-section. This approach, combined with a proper description of elastic forces, led to higher accuracy and convergence rates than those observed for the two-node elements.

2.3.1 Kinematics of the ANCF beam elements

Like typical three-dimensional finite element formulations, the ANCF uses shape functions and inertial coordinates. The position vector of an arbitrary material point in inertial frame $\mathcal{I}$ is interpolated as

$$\underline{r} = \underline{\underline{S}}_m(\alpha_1, \alpha_2, \alpha_3)\underline{e}, \tag{7}$$

where matrix $\underline{\underline{S}}_m$ stores the shape functions expressed in terms of the element local coordinates α_1, α_2, and α_3, and array $\underline{e}$ stores the nodal coordinates. Array $\underline{e}$ is partitioned as $\underline{e} = \{\underline{e}^{(1)T}, \underline{e}^{(2)T}, \ldots, \underline{e}^{(n)T}\}$, where n is the number of nodes of the element. For fully parameterized ANCF beam elements the nodal coordinates are

$$\underline{e}^{(i)} = \begin{bmatrix} \underline{r}^{(i)T} & \underline{r}_{,1}^{(i)T} & \underline{r}_{,2}^{(i)T} & \underline{r}_{,3}^{(i)T} \end{bmatrix}^T, \tag{8}$$

where $\underline{r}^{(i)}$ is the inertial position of node i, $\underline{r}_{,1}^{(i)}$ the longitudinal slope vector, and $\underline{r}_{,2}^{(i)}$ and $\underline{r}_{,3}^{(i)}$ the transverse slope vectors used to define cross-sectional orientations and deformations. Notation $(\cdot)_{,j}$ indicates a derivative with respect to coordinate α_j, *i.e.*, $\underline{r}_{,j} = \partial \underline{r}/\partial \alpha_j$ for $j = 1, 2, 3$.

2.3.2 Two-node ANCF beam element

In this section, the two-node beam element introduced by Dufva *et al.* [32] is summarized succinctly. The kinematic description of the element is similar to that proposed by Yakoub and Shabana [35], while the strain energy is different. The rotation of the cross-section is defined using linear interpolation over the beam's span. In the case of the two-node element, transverse shear deformations vary linearly over the beam length to alleviate shear locking [32]. For this reason, the kinematics

uses local coordinate systems that describe distinct cross-section rotations due to bending and shear deformations. The position vector of a material point in the beam element is expressed as

$$\underline{r}_p = \underline{r}_0 + \underline{\underline{R}}_3 \underline{\underline{A}}_2 \underline{y} + \underline{\underline{R}}_2 \underline{\underline{A}}_3 \underline{z}, \tag{9}$$

where $\underline{r}_0 = \underline{r}(\alpha_1, 0, 0)$ is the position vector of the beam's reference line and vectors $\underline{y} = \{0, \alpha_2, 0\}^T$ and $\underline{z} = \{0, 0, \alpha_3\}^T$ define the plane of the cross-section. The position vector of a material point is defined using third-order interpolation. The shape functions for the element are defined in terms of the non-dimensional axial variable $\xi = 2\alpha_1/L$ and transverse variables $\eta = 2\alpha_2/H$ and $\zeta = 2\alpha_3/W$, where L, H, and W are the element length, height, and width, respectively. For the present element, the shape functions are

$$\begin{aligned} S_1 &= (\xi+1)(\xi-2)^2/4, & S_2 &= L\xi(\xi-2)^2/8, \\ S_3 &= H\eta(\xi+2)/4, & S_4 &= W\zeta(\xi+2)/4, \\ S_5 &= \xi^2(\xi+3)/4, & S_6 &= L\xi^2(\xi-2)/8, \\ S_7 &= H\xi\eta/4, & S_8 &= W\xi\zeta/4. \end{aligned} \tag{10}$$

Rotation matrices $\underline{\underline{A}}_2$ and $\underline{\underline{A}}_3$ describe the rotations of the cross-section due to bending deformations [32] about the local α_2- and α_3-axes, respectively. The first rotation tensor is written as $\underline{\underline{A}}_2 = [\bar{t}_2, \bar{n}_2, \bar{b}_2]$, where the tangent to the reference line is $\bar{t}_2 = \underline{r}_{,1}/\|\underline{r}_{,1}\|$, $\bar{b}_2 = (\underline{r}_{,1} \times \underline{r}_{,2})/(\|\underline{r}_{,1} \times \underline{r}_{,2}\|)$ and $\bar{n}_2 = (\bar{b}_2 \times \underline{r}_{,1})/(\|\bar{b}_2 \times \underline{r}_{,1}\|)$. Similarly, the second rotation tensor is $\underline{\underline{A}}_3 = [\bar{t}_2, \bar{n}_3, \bar{b}_3]$, where $\bar{n}_3 = (\underline{r}_{,3} \times \underline{r}_{,1})/(\|\underline{r}_{,3} \times \underline{r}_{,1}\|)$ and $\bar{b}_3 = (\underline{r}_{,1} \times \bar{n}_3)/(\|\underline{r}_{,1} \times \bar{n}_3\|)$.

Rotation tensor $\underline{\underline{R}}_2$ gives the additional rotation due to transverse shear deformation along the local α_2-axis. To obtain this rotation tensor, the kinematics of the ANCF are used to approximate the shear angle in terms of the slope vectors as $\gamma_2 \approx \sin\gamma_2 = (\underline{r}_{,1}^T \underline{r}_{,3})/(\|\underline{r}_{,1}\|\|\underline{r}_{,3}\|)$. The nodal shear strains are denoted $\gamma_2^{(1)}$ and $\gamma_2^{(2)}$ and to alleviate shear locking, the shear angle within the element is interpolated using linear shape functions, $\gamma_2 = N_1\gamma_2^{(1)} + N_2\gamma_2^{(2)}$, where N_1 and N_2 are the conventional linear shape functions. Finally, for small shear angles, the following approximations are made: $\underline{\underline{R}}_2 \approx \underline{\underline{I}} + \gamma_2 \tilde{b}_2^*$. A similar development yields rotation tensor $\underline{\underline{R}}_3$ that gives the additional rotation due to transverse shear deformation along the local α_3-axis. Nodal values are evaluated as $\gamma_3 \approx \sin\gamma_3 = -(\underline{r}_{,1}^T \underline{r}_{,2})/(\|\underline{r}_{,1}\|\|\underline{r}_{,2}\|)$ and linear interpolation of nodal values leads to $\underline{\underline{R}}_z \approx \underline{\underline{I}} + \gamma_z \tilde{b}_3^*$.

The components of the Green-Lagrange strain tensor are obtained readily as

$$\begin{aligned} \epsilon_{xx} &= (\underline{r}_{p,1}^T \underline{r}_{p,1} - 1)/2, & \epsilon_{yy} &= (\underline{r}_{,2}^T \underline{r}_{,2} - 1)/2, & \epsilon_{zz} &= (\underline{r}_{,3}^T \underline{r}_{,3} - 1)/2, \\ \epsilon_{xy} &= (\underline{r}_{p,1}^T \underline{r}_{p,2})/2, & \epsilon_{xz} &= (\underline{r}_{p,1}^T \underline{r}_{p,3})/2, & \epsilon_{yz} &= (\underline{r}_{p,2}^T \underline{r}_{p,3})/2. \end{aligned} \tag{11}$$

For a beam made of a homogeneous isotropic material of Young's modulus E and shear modulus G, the strain energy stored in one beam element of volume V is

$$A = \frac{1}{2} \int_V \left[E(\epsilon_{xx}^2 + \epsilon_{yy}^2 + \epsilon_{zz}^2) + 4G(k_2\epsilon_{xz}^2 + k_3\epsilon_{xy}^2 + \epsilon_{yz}^2) \right] \, \mathrm{d}V, \tag{12}$$

where k_2 and k_3 are the shear correction factors.

2.3.3 Three-node ANCF beam element

The second ANCF element to be used in this study is the three-node ANCF beam element introduced by Nachbagauer *et al.* [33], in which the position vector and sectional rotations are interpolated quadratically and linearly, respectively, over the element. Due to a different definition of the strain energy and an improved integration scheme, the accuracy and convergence order of this three-node element are better than those of the two-node element described in the previous section.

This three-node element has a long history. Initially, the choice of degrees of freedom was proposed by Kerkkänen *et al.* [36] and García-Vallejo *et al.* [37], in which longitudinal slope vectors were omitted. The strain components are identical to those presented by Gerstmayr *et al.* [38] and Nachbagauer *et al.* [39]. A two-node version of the element was proposed by Matikainen *et al.* [40]. Additional elements without longitudinal slope vectors are described by Matikainen *et al.* [41]. In addition to these changes in kinematics, the strain energy expression proposed by Simo was introduced in two- and three-dimensional ANCF by Gerstmayr *et al.* [38] and Nachbagauer *et al.* [39], respectively.

In Nachbagauer *et al.* [33], the kinematics of the beam element is defined using three nodes, each of which has nine degrees of freedom. The vector of nodal coordinates for the beam element is expressed as

$$\underline{e}^T = \left\{ \underline{r}^{(1)T} \quad \underline{r}_{,2}^{(1)T} \quad \underline{r}_{,3}^{(1)T} \quad \underline{r}^{(2)T} \quad \underline{r}_{,2}^{(2)T} \quad \underline{r}_{,3}^{(2)T} \quad \underline{r}^{(3)T} \quad \underline{r}_{,2}^{(3)T} \quad \underline{r}_{,3}^{(3)T} \right\}, \tag{13}$$

where $\underline{r}^{(i)}$ are the inertial position vectors of the nodes, and $\underline{r}_{,2}^{(i)}$ and $\underline{r}_{,3}^{(i)}$ the transverse slope vectors that define the orientation of the beam's cross-section. The shape functions for the element are written as

$$\begin{aligned} S_1 = \xi(\xi-1)/2, \quad S_2 = H\eta S_1, \quad S_3 = W\zeta S_1, \\ S_4 = \xi(\xi+1)/2, \quad S_5 = H\eta S_4, \quad S_6 = W\zeta S_4, \\ S_7 = 1-\xi^2, \quad S_8 = H\eta S_7, \quad S_9 = W\zeta S_7, \end{aligned} \tag{14}$$

and matrix $\underline{\underline{S}}_m$ defined by eq. (7) becomes $\underline{\underline{S}}_m = [S_1\underline{\underline{I}}, \ldots, S_9\underline{\underline{I}}]$.

The kinematics of the element rely on a single rotation tensor, $(\underline{\underline{R}}\,\underline{\underline{R}}_0) = \left[\bar{b}_1, \bar{b}_2, \bar{b}_3\right]$, where unit vectors $\bar{b}_1$, $\bar{b}_2$, and $\bar{b}_3$ are shown in fig. 1. In the present formulation, the axial unit vector $\bar{b}_1 = (\underline{r}_{,2} \times \underline{r}_{,3})/\|\underline{r}_{,2} \times \underline{r}_{,3}\|$ and the transverse unit vectors are selected as $\bar{b}_2 = \underline{r}_{,2}/\|\underline{r}_{,2}\|$, and $\bar{b}_3 = (\underline{r}_{,3} \times \bar{b}_1)/\|\underline{r}_{,3} \times \bar{b}_1\|$. The sectional strain components are now given by eq. (1), where $\underline{x}_0' + \underline{u}' = \underline{r}_{,1}$.

The strain energy stored in the beam is given by eq. (4), where the section stiffness matrix is selected as $\underline{\underline{\mathcal{D}}}^* = \mathrm{diag}(S, K_{22}, K_{33}, H_{11}, H_{22}, H_{33})$, where $S = E\mathcal{A}$ is axial stiffness, $H_{22} = EI_2$ and $H_{33} = EI_3$ the bending stiffnesses about unit vectors $\bar{b}_2$ and $\bar{b}_3$, respectively, and $H_{11} = GJ$ is torsional stiffness. The shear stiffnesses are $K_{22} = G\mathcal{A}k_2$ and $K_{33} = G\mathcal{A}k_3$ along unit vectors $\bar{b}_2$ and $\bar{b}_3$, respectively, where k_2 and k_3 are the shear correction factors.

In the present formulation, the transverse slope vectors, $\underline{r}_{,2}$ and $\underline{r}_{,3}$, do not remain unit vectors nor do they remain mutually orthogonal. Hence, they describe cross-sectional deformations and neglecting Poisson's effect, the associated strain energy is found as

$$A_{csd} = \frac{1}{2}\int_0^L \left[E\mathcal{A}(E_{yy}^2 + E_{zz}^2) + 2G\mathcal{A}E_{yz}^2\right] \, \mathrm{d}\alpha_1, \tag{15}$$

where $E_{yy} = (\underline{r}_{,2}^T\underline{r}_{,2} - 1)/2$ and $E_{zz} = (\underline{r}_{,3}^T\underline{r}_{,3} - 1)/2$ are the in-plane strains and $E_{yz} = \underline{r}_{,2}^T\underline{r}_{,3}/2$ the in-plane shear strain, all computed at the beam's reference line. The beam's total strain energy is the sum of two components, A and A_{csd}, defined by eqs (4) and (15), respectively. To alleviate locking, selective integration is used in the element: a two-point Gauss and a three-point Lobatto integration schemes were used to integrate the strain energies defined by eqs. (4) and (15), respectively.

2.4 Summary

This section has summarized in a very succinct manner three beam element formulations that are widely used in flexible multibody dynamics simulations. The geometrically exact beam formulation summarized in section 2.2 is a classical formulation that has been used for decades; initially proposed by Simo *et al.* [5, 6], then by Borri and Merlini [7], Danielson and Hodges [8, 9], and Bauchau and

Hong [10, 11, 12]. These formulations are characterized by the sectional strains and strain energy defined by eqs. (1) and (4), respectively. The various authors mentioned above have used different shape functions and various integration schemes.

Furthermore, different parameterizations of rotation and many rational techniques for their interpolation have been proposed [42, 43, 44]. It is also possible to use a redundant representation of rotation, such as that proposed by Betsch *et al.* [45, 46, 47], who used nine degrees of freedom to represent rotation. Six constraint equations are then imposed, because three independent parameters only are required to represent three-dimensional rotations. Yet all these formulations use the sectional strains and strain energy definitions that characterize geometrically exact beams.

The ANCF element presented in section 2.3.2 is rooted in the original formulation of Shabana and Yakoub [34, 35] and presents a radical departure from the GEBF. Indeed, rather than using the sectional strains and strain energy defined by eqs. (1) and (4), respectively, it is based on three-dimensional expressions for the Green-Lagrange strain components and strain energy defined by eqs. (11) and (12), respectively. Here again, various authors have used different shape functions and various integration schemes.

Finally, the formulation presented in section 2.3.3 can be viewed as a GEBF with a redundant representation of rotation. Indeed, it uses the sectional strains and strain energy defined by eqs. (1) and (4), respectively, that characterize the GEBF. The two transverse slope vectors use six degrees of freedom to represent three rotation components. Instead of imposing holonomic constraints, this formulation enforces these three constraints via the penalty method. Indeed, eq. (15) can be interpreted as a penalty term that enforces the unit norms and mutual othogonality of the transverse slope vectors using penalty coefficients $E\mathcal{A}$ and $G\mathcal{A}$, respectively.

3 Experimental validation

The various formulations presented in the previous section will be validated by comparing their predictions against the measurements of the Princeton beam experiment.

3.1 The Princeton beam experiment

The Princeton beam experiment [3, 4] is a study of the large displacement and rotation behavior of a simple cantilevered beam under a gravity tip load. A straight aluminum (T 7075) beam of length $L = 0.508$ m with a rectangular cross-section of nominal thickness $t = 3.175$ mm and nominal height $h = 12.7$ mm was cantilevered at its root and subjected to a static concentrated load P at its tip.

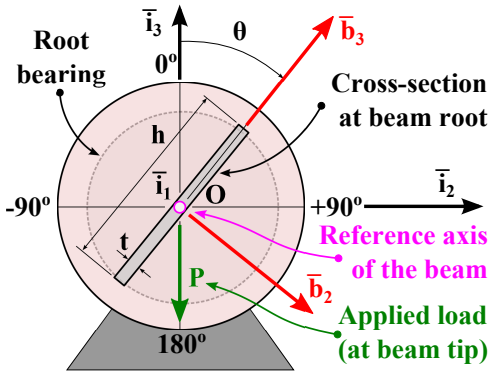

Figure 2: Configuration of the Princeton beam experiment.

Figure 2 shows an end-view of the test set-up. An inertial frame of reference is selected as $\mathcal{F}^I = [\mathbf{O}, \mathcal{I} = (\bar{\imath}_1, \bar{\imath}_2, \bar{\imath}_3)]$ and material frame $\mathcal{F}^B = [\mathbf{O}, \mathcal{B} = (\bar{b}_1, \bar{b}_2, \bar{b}_3)]$ is attached at the beam's

root section, which is cantilevered into a bearing that allows rotation of the beam about its reference axis by an angle θ, called the "loading angle." The gravity load applied at the beam tip is acting in the opposite direction of unit vector $\bar{\imath}_3$. Variation of the loading angle from 0 to 90 degrees yields a wide range of nonlinear problems where torsion and bending in two directions are coupled.

Experimental results [3] consist of measurements of the beam's tip deflection along the material unit vectors $\bar{b}_2$ and $\bar{b}_3$, denoted u_2 and u_3, respectively, and called the "flapwise" and "chordwise displacements," respectively. Furthermore, the beam's tip twist was also measured. Let $\underline{\underline{R}}^E = \left[\bar{b}_1^E, \bar{b}_2^E, \bar{b}_3^E\right]$ denote the rotation tensor of the beam's tip cross-section. In the absence of tip load, $\underline{\underline{R}}^E(P=0) = \left[\bar{b}_1^E, \bar{b}_2^E, \bar{b}_3^E\right]$, where $\bar{b}_3^{ET} = \left\{0, \sin\theta, \cos\theta\right\}$, and it then follows that $\theta = \arctan(R_{23}^E(P=0)/R_{33}^E(P=0))$. Under a tip load P, the orientation of the tip section is defined as $\arctan(R_{23}^E(P)/R_{33}^E(P))$ and the beam's tip twist is defined as

$$\phi = \arctan(\frac{R_{23}^E}{R_{33}^E}) - \theta. \tag{16}$$

The procedure used to measure the twist angle experimentally is detailed in the report by Dowell and Traybar [3].

Data was acquired at loading angles of $\theta = 0, \pm 15, \pm 30, \pm 45, \pm 60, \pm 75, \pm 90$, and 180 degrees. For a perfect system, symmetry implies that the absolute values of the tip displacements and twist should be identical for loading angles $\pm\theta$. In the experimental setting, these measurements differed, providing an estimate of their accuracy. Three loading conditions were used, $P_1 = 4.448$ N (1 lb), $P_2 = 8.896$ N (2 lbs), and $P_3 = 13.345$ N (3 lbs). Figures 3, 4, and 5 show the experimental measurements for the absolute value of the tip flapwise displacement, chordwise displacement, and twist, respectively. Symbols indicate the average of the measurements and error bars are also provided.

Note that the Dowell and Traybar report [3] provides no measurements for loading condition P_2 at loading angles $\theta = 75$ and 90 degrees and for loading condition P_3 at loading angles $\theta = 60$, 75, and 90 degrees. A cursory look at fig. 3 reveals that those loading cases would result in large flapwise deflections, which could generate permanent plastic deformations in the beam. It is likely that the authors of the study did not want to damage the test article and hence, did not acquire data at those loading conditions.

3.2 Correlation using linear theory

The linear solution of the problem is found using the shear deformable beam theory described in structural analysis textbooks such as that of Bauchau and Craig [19]. The tip transverse displacement components are

$$u_2^T = \left[\frac{PL^3}{3H_{33}} + \frac{PL}{K_{22}}\right]\sin\theta, \tag{17a}$$

$$u_3^T = \left[\frac{PL^3}{3H_{22}} + \frac{PL}{K_{33}}\right]\cos\theta. \tag{17b}$$

Of course, for the linear theory, the tip twist vanishes.

For $\theta = 0$ or 180 and $\theta = \pm 90$, the beam undergoes planar deformation and elementary formulæ of Timoshenko beam theory (17) provide the tip deflection in the linear regime. Using the Young's modulus of T 7075 aluminum as $E = 71.7$ GPa and Poisson's ratio $\nu = 0.31$, hand calculations yield $u_2^T = 5.004$ and $u_3^T = 80.034$ mm for the chordwise and flapwise tip displacements, respectively, at loading level P_1. This compares favorably with experimental measurements of $u_2^T = 5.3594$ and $u_3^T = 77.635$ mm, respectively, resulting in -6.6 and +3.1% error, respectively. In this effort, the

dimensions of the cross-section were adjusted slightly to achieve good correlation between measurements and predictions of linear theory in these two cases. The following data was used for this correlation effort. Beam dimensions: $L = 0.508$ m, $t = 3.2024$ mm and height $h = 12.377$ mm; material properties: $E = 71.7$ GPa, Poisson's ratio $\nu = 0.31$, and shear modulus $G = E/2(1+\nu)$ $= 27.37$ GPa.

Because the distributed mass of the beam is far smaller than the applied tip weight, it was neglected in the simulations. Consequently, rather than rotating the beam, it was kept at a fixed, vertical orientation at the root, and the direction of the applied load was varied from 0 to 90 degrees.

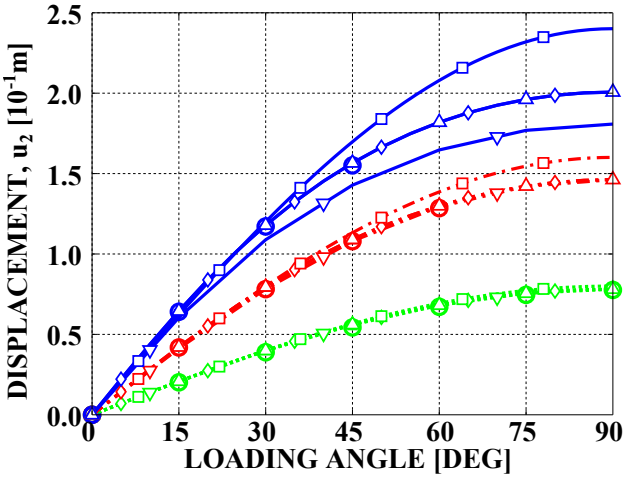

Figure 3: Flapwise displacement at the beam tip versus loading angle for three loading conditions. Experimental measurements: ◯ with error bars. Predictions: Linear solution (□), GEBF (△), two-node ANCF (▽), and three-node ANCF (◇). Loading condition: P_1, dashed-dotted line, P_2, dotted line, P_3 solid line.

Figures 3 and 4 show the flapwise and chordwise displacements, respectively, predicted by the linear theory expressed by eq. (17a) and (17b), respectively. The flapwise displacements are predicted accurately for the smaller applied load level, P_1, but significant discrepancies are observed for the P_2 and P_3 loading levels.

In contrast, the chordwise displacement predictions shown in fig. 4 are poor, even for the lowest loading level. At a loading angle of 45 degrees, the linear solution underpredicts the measured displacement by about 27% for loading level P_3. Note that the linear predictions decrease monotonically as the loading angle increases, while the experiments show an initial rise before a steeper decline. This behavior, which is particularly noticeable for the highest loading level, stems from the nonlinear coupling between torsion and chordwise bending, a phenomenon that is not captured by linear theory.

Of course, linear theory predicts a vanishing tip twist angle because for the present configuration, twisting is attributable to nonlinear effects entirely. For this experimental setup, torsion is the phenomenon exhibiting the most pronounced nonlinear behavior. Tip twist, *per se*, is due to nonlinear effects only, and the indirect effect of twisting on chordwise bending is very important, as shown in fig. 4.

3.3 Correlation using GEBF

The GEBF uses sectional stiffness parameters as input data. These parameters were computed from the physical data given in the previous section and the following values were used: axial stiffness $S = 2.84$ MN, chordwise bending stiffness $H_{22} = 36.28$ N·m^2, flapwise bending stiffness $H_{33} = 2.43$ N·m^2, torsion stiffness $H_{11} = 3.10$ N·m^2, flapwise shear stiffness $K_{22} = 0.64$ MN, and

chordwise shear stiffness $K_{33} = 0.90$ MN. The stiffness parameters of the beam's rectangular cross-section were evaluated using the three-dimensional elasticity solution developed by Bauchau and Han [48]. If the strain energy stored per unit span of the beam is evaluated with the help of these stiffness coefficients, it is identical to that stored in the three-dimensional structure of infinite length. Different shear coefficients result for the beam's flapwise and chordwise directions.

The beam was modeled with 12 four-node elements. Each node features six degrees of freedom, three displacement and three rotation components. Cubic interpolation functions were used for both displacement and rotation fields. Interpolation of the rotation field is based on the interpolation of the relative rotation parameter vector [44]. To eliminate shear locking effects, a three-Gauss point reduced integration scheme was used.

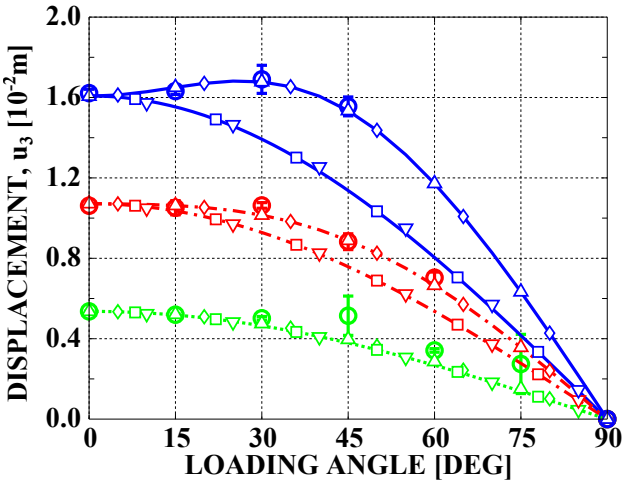

Figure 4: Chordwise displacement at the beam tip versus loading angle for three loading conditions. Experimental measurements: ◯ with error bars. Predictions: Linear solution (□), GEBF (△), two-node ANCF (▽), and three-node ANCF (♢). Loading condition: P_1, dashed-dotted line, P_2, dotted line, P_3 solid line.

The predictions of the GEBF for the three loading cases are shown in figs 3, 4, and 5 that depict the tip flapwise displacement, chordwise displacement, and twist, respectively. For all loading cases and loading angles, excellent correlation with experiment is observed.

3.4 Correlation using two-node ANCF beam element

Next, the predictions of the two-node ANCF beam element were correlated with experimental results. The beam was modeled with eight two-node elements. Twelve degrees of freedom are defined at each node and include three displacement and nine slope components that describe cross-sectional rotation and deformation. As explained in section 2.3.2, each two-node element employs cubic and linear shape functions in the axial and transverse directions, respectively. In this study, the beam has a rectangular cross-section and volume integrals were performed using full Gaussian integration: four points in the axial direction and 2×2 points over the cross-section.

The predictions the two-node ANCF beam element for the three loading cases are shown in figs 3, 4, and 5 that depict tip flapwise displacement, chordwise displacement, and twist, respectively. For the tip flapwise displacement, the predictions are in good agreement with the measured data. In contrast, for the tip chordwise displacement and twist, poor correlation is observed. The predictions are close to those of linear theory, because the two-node element does not predict torsion correctly, as shown in fig 5.

3.5 Correlation using three-node ANCF beam element

Finally, the predictions of the three-node ANCF beam element were correlated with experimental results. The beam was modeled with eight three-node elements. Nine degrees of freedom are defined at each node and include three displacement and six slope components that describe cross-sectional rotation. Each element uses quadratic and linear shape functions in the axial and transverse directions, respectively. For the three-node beam, line integrals were evaluated using selective Gaussian integration: a two-point Gauss and a three-point Lobatto integration schemes were used to integrate the strain energies defined by eqs. (4) and (15), respectively.

The predictions for the three-node ANCF beam element for the three loading cases are shown in figs 3, 4, and 5 that depict tip flapwise displacement, chordwise displacement, and twist, respectively. For all loading cases and loading angles, excellent correlation with experiment data is observed. Note that the predictions of the three-node ANCF element are nearly identical to those of the GEBF. This is to be expected since both formulations are nearly identical.

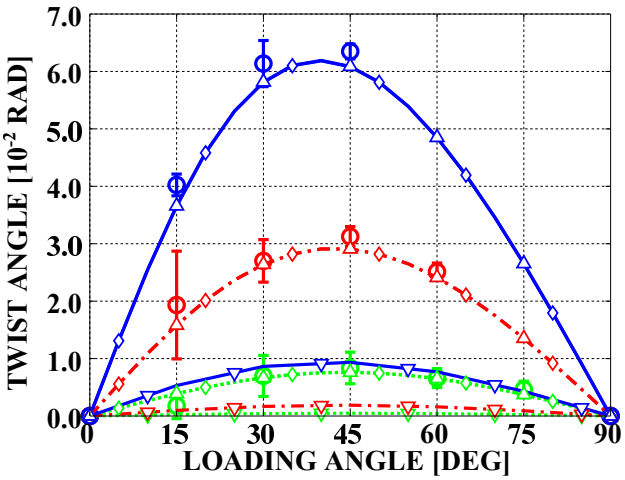

Figure 5: Twist at the beam tip versus loading angle for three loading conditions. Experimental measurements: ◯ with error bars. Predictions: GEBF (△), two-node ANCF (▽), and three-node ANCF (♢). Loading condition: P_1, dashed-dotted line, P_2, dotted line, P_3 solid line. Note that the linear solution predicts a vanishing twist angle.

3.6 Convergence study for the three beam elements

To further compare the three elements used in this paper, a convergence study is presented next. Four different cases will be compared: the GEBF 3-node element (*i.e.*, with quadratic shape functions), the GEBF 4-node element (*i.e.*, with cubic shape functions), the two-node ANCF element, and three-node ANCF element. For each element, simulations were run with increasingly finer meshes for loading case P_3. In each case, the reference solution was selected as that obtained with the finest mesh and relative errors with respect to the reference solutions were then obtained.

Figure 6 shows the result of the convergence study for tip flapwise displacement at loading angle $\theta = 0$ deg and fig. 7 the corresponding results at loading angle $\theta = 30$ deg. Finally, fig. 8 shows the relative error in tip chordwise displacement at loading angle $\theta = 30$ deg. Note that all results are presented on log-log plots.

As expected from the studies of Romero [16] and Bauchau *et al.* [18], at equal numbers of degrees of freedom, the predictions of the GEBF elements are more accurate than those of the ANCF elements.

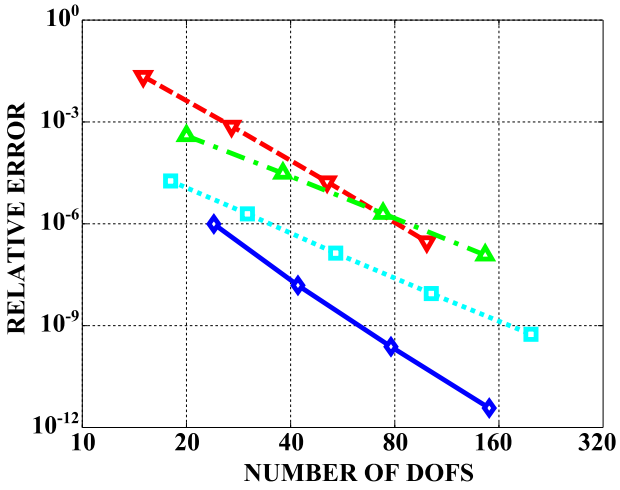

Figure 6: Relative error in the tip flapwise displacement at loading angle $\theta = 0$ deg, loading conditions P_3: GEBF 3-node element ($\square$), GEBF 4-node element ($\diamond$), two-node ANCF ($\bigtriangledown$), and three-node ANCF ($\bigtriangleup$).

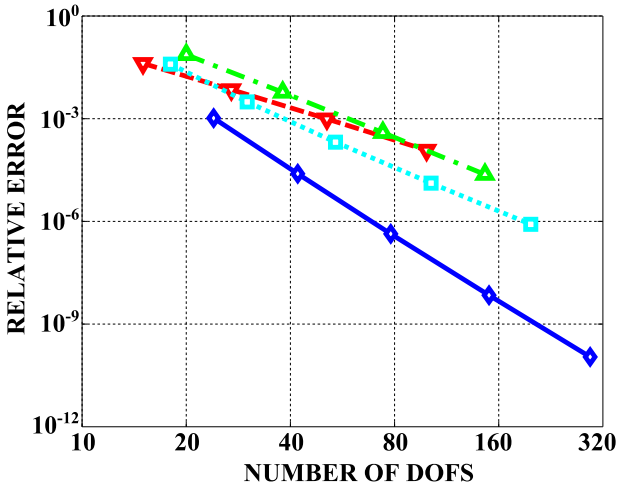

Figure 7: Relative error in tip flapwise displacement at loading angle $\theta = 30$ deg, loading conditions P_3: GEBF 3-node element ($\square$), GEBF 4-node element ($\diamond$), two-node ANCF ($\bigtriangledown$), and three-node ANCF ($\bigtriangleup$).

4 Conclusions

In this paper, the accuracies of the geometrically exact beam and absolute nodal coordinate formulations were assessed by comparing their respective predictions against experimental data. In the experiment, a cantilever beam was subjected to coupled flap, lag, and twist deformations.

The predictions of the two-node beam element based on the ANCF did not correlate well with the experimental data. In fact, for the tip chordwise displacement and twist, predictions were close to those of linear theory. These poor predictions stemmed from the inability of this formulation to capture the torsional behavior of the beam accurately. The inadequate modeling of torsional behavior resulted, in turn, in poor predictions of the coupled chordwise displacements that were found to be up to 27% in error compared to experimental measurements. This two-node beam element is rooted in the original ANCF proposed by Shabana and Yakoub. Although accurate predictions can be obtained for planar beam problems, this study suggests that this formulation should not be used for three-dimensional beams undergoing coupled bending and torsion.

The numerical predictions of the GEBF and of the recently proposed three-node element based

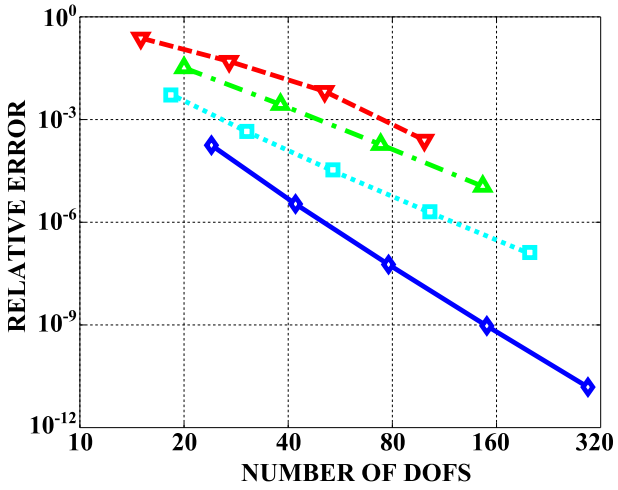

Figure 8: Relative error in tip chordwise displacement at loading angle $\theta = 30$ deg, loading conditions P_3: GEBF 3-node element ($\square$), GEBF 4-node element ($\diamond$), two-node ANCF ($\bigtriangledown$), and three-node ANCF ($\bigtriangleup$).

on the ANCF agree well with the experimental data at all loading angles and for the three loading cases. Although the numerical implementations of the elements differ, both elements share the sectional strain and strain energy definitions that characterize the GEBF. The GEBF presented here uses a minimum set of variables, three nodal displacements and rotations. In contrast, the three-node ANCF element uses a redundant set of coordinates: six degrees of freedom are used to represent rotation of the cross-section. Constraints are enforced via the penalty method.

This study demonstrates the crucial need for thorough validation of the beam elements used for the simulation of flexible multibody systems before they are used to solve practical problems. Comparison with available experimental data seems indispensable. Predictions of the original absolute nodal coordinate formulation have been widely presented in the literature, primarily for planar problems, yet this study shows that this formulation cannot handle three-dimensional beam problems accurately.

5 Acknowledgements

The authors would like to thank the Academy of Finland (Application No. 259543) for supporting Marko K. Matikainen.

References

[1] J.C. Houbolt and G.W. Brooks. Differential equations of motion for combined flapwise bending, chordwise bending, and torsion of twisted nonuniform rotor blades. Technical Report 1348, NACA Report, 1958.

[2] D.H. Hodges and E.H. Dowell. Nonlinear equations of motion for the elastic bending and torsion of twisted nonuniform rotor blades. Technical report, NASA TN D-7818, 1974.

[3] E.H. Dowell and J.J. Traybar. An experimental study of the nonlinear stiffness of a rotor blade undergoing flap, lag, and twist deformations. Aerospace and Mechanical Science Report 1257, Princeton University, 1975.

[4] E.H. Dowell, J.J. Traybar, and D.H. Hodges. An experimental-theoretical correlation study of non-linear bending and torsion deformations of a cantilever beam. *Journal of Sound and Vibration*, 50(4):533–544, February 1977.

[5] J.C. Simo. A finite strain beam formulation. The three-dimensional dynamic problem. Part I. *Computer Methods in Applied Mechanics and Engineering*, 49(1):55–70, 1985.

[6] J.C. Simo and L. Vu-Quoc. A three-dimensional finite strain rod model. Part II: Computational aspects. *Computer Methods in Applied Mechanics and Engineering*, 58(1):79–116, 1986.

[7] M. Borri and T. Merlini. A large displacement formulation for anisotropic beam analysis. *Meccanica*, 21:30–37, 1986.

[8] D.A. Danielson and D.H. Hodges. Nonlinear beam kinematics by decomposition of the rotation tensor. *Journal of Applied Mechanics*, 54(2):258–262, 1987.

[9] D.A. Danielson and D.H. Hodges. A beam theory for large global rotation, moderate local rotation, and small strain. *Journal of Applied Mechanics*, 55(1):179–184, 1988.

[10] O.A. Bauchau and C.H. Hong. Finite element approach to rotor blade modeling. *Journal of the American Helicopter Society*, 32(1):60–67, 1987.

[11] O.A. Bauchau and C.H. Hong. Large displacement analysis of naturally curved and twisted composite beams. *AIAA Journal*, 25(11):1469–1475, 1987.

[12] O.A. Bauchau and C.H. Hong. Nonlinear composite beam theory. *Journal of Applied Mechanics*, 55:156–163, March 1988.

[13] A.A. Shabana and R.A. Wehage. A coordinate reduction technique for dynamic analysis of spatial substructures with large angular rotations. *Journal of Structural Mechanics*, 11(3):401–431, March 1983.

[14] O.P. Agrawal and A.A. Shabana. Application of deformable-body mean axis to flexible multibody system dynamics. *Computer Methods in Applied Mechanics and Engineering*, 56(2):217–245, 1986.

[15] A.A. Shabana. Flexible multibody dynamics: Review of past and recent developments. *Multibody System Dynamics*, 1(2):189–222, June 1997.

[16] I. Romero. A comparison of finite elements for nonlinear beams: the absolute nodal coordinate and geometrically exact formulations. *Multibody System Dynamics*, 20:51–68, 2008.

[17] J. Gerstmayr, H. Sugiyama, and A. Mikkola. An overview on the developments of the absolute nodal coordinate formulation. In *Proceedings of the Second Joint International Conference on Multibody System Dynamics*, Stuttgart, Germany, May 2012.

[18] O.A. Bauchau, S.L. Han, A. Mikkola, and M.K. Matikainen. Comparison of the absolute nodal coordinate and geometrically exact formulations for beams. *Multibody System Dynamics*, 32(1):67–85, June 2014.

[19] O.A. Bauchau and J.I. Craig. *Structural Analysis with Application to Aerospace Structures*. Springer, Dordrecht, Heidelberg, London, New-York, 2009.

[20] S.P. Timoshenko. On the correction factor for shear of the differential equation for transverse vibrations of bars of uniform cross-section. *Philosophical Magazine*, 41:744–746, 1921.

[21] S.P. Timoshenko. On the transverse vibrations of bars of uniform cross-section. *Philosophical Magazine*, 43:125–131, 1921.

[22] E. Reissner. The effect of transverse shear deformation on the bending of elastic plates. *Zeitschrift für angewandte Mathematik und Physik*, 12:A.69–A.77, 1945.

[23] R.D. Mindlin. Influence of rotatory inertia and shear on flexural motions of isotropic elastic plates. *Journal of Applied Mechanics*, 18:31–38, 1951.

[24] E. Reissner. On one-dimensional finite-strain beam theory: the plane problem. *Zeitschrift für angewandte Mathematik und Physik*, 23:795–804, 1972.

[25] E. Reissner. On one-dimensional large-displacement finite-strain beam theory. *Studies in Applied Mathematics*, 52:87–95, 1973.

[26] E. Reissner. On finite deformations of space-curved beams. *Zeitschrift für angewandte Mathematik und Physik*, 32:734–744, 1981.

[27] L.E. Malvern. *Introduction to the Mechanics of a Continuous Medium*. Prentice Hall, Inc., Englewood Cliffs, New Jersey, 1969.

[28] D.H. Hodges. *Nonlinear Composite Beam Theory*. AIAA, Reston, Virginia, 2006.

[29] O.A. Bauchau. *Flexible Multibody Dynamics*. Springer, Dordrecht, Heidelberg, London, New-York, 2011.

[30] V. Giavotto, M. Borri, P. Mantegazza, G. Ghiringhelli, V. Carmaschi, G.C. Maffioli, and F. Mussi. Anisotropic beam theory and applications. *Computers & Structures*, 16(1-4):403–413, 1983.

[31] O.A. Bauchau and S.L. Han. Three-dimensional beam theory for flexible multibody dynamics. *Journal of Computational and Nonlinear Dynamics*, 9(4):041011 (12 pages), 2014.

[32] K.E. Dufva, J.T. Sopanen, and A.M. Mikkola. A three-dimensional beam element based on a cross-sectional coordinate system approach. *Nonlinear Dynamics*, 43(4):311–327, 2005.

[33] K. Nachbagauer, P. Gruber, and J. Gerstmayr. Structural and continuum mechanics approaches for a 3d shear deformable ancf beam finite element: Application to static and linearized dynamic examples. *ASME Journal of Computational and Nonlinear Dynamics*, 8(2):021004, 2013.

[34] A.A. Shabana and R.Y. Yakoub. Three dimensional absolute nodal coordinate formulation for beam elements: Theory. *ASME Journal of Mechanical Design*, 123:606–613, 2001.

[35] R.Y. Yakoub and A.A. Shabana. Three dimensional absolute nodal coordinate formulation for beam elements: Implementation and applications. *ASME Journal of Mechanical Design*, 123:614–621, 2001.

[36] K. S. Kerkkänen, J. T. Sopanen, and A. M. Mikkola. A linear beam finite element based on the absolute nodal coordinate formulation. *Journal of Mechanical Design*, 127(4):621–630, 2005.

[37] D. García-Vallejo, A. Mikkola, and J.L. Escalona. A new locking-free shear deformable finite element based on absolute nodal coordinates. *Nonlinear Dynamics*, 50(1-2):249–264, 2007.

[38] J. Gerstmayr, M.K. Matikainen, and A.M. Mikkola. A geometrically exact beam element based on the absolute nodal coordinate formulation. *Multibody System Dynamics*, 20(4):359–384, 2008.

[39] K. Nachbagauer, S.A. Pechstein, H. Irschik, and J. Gerstmayr. A new locking free formulation for planar, shear deformable, linear and quadratic beam finite elements based on the absolute nodal coordinate formulation. *Journal of Multibody System Dynamics*, 26(3):245–263, 2011.

[40] M.K. Matikainen, R. von Hertzen, A.M. Mikkola, and J. Gerstmayr. Elimination of high frequencies in the absolute nodal coordinate formulation. *Proceedings of the Institution of Mechanical Engineers, Part K: Journal of Multi-body Dynamics*, 224(1):103–116, 2010.

[41] M.K. Matikainen, O. Dmitrochenko, and A.M. Mikkola. Beam elements with trapezoidal cross-section deformation modes based on the absolute nodal coordinate formulation. In *International Conference of Numerical Analysis and Applied Mathematics*, Rhodes, Greece, 19-25 September 2010.

[42] M.A. Crisfield and G. Jelenić. Objectivity of strain measures in the geometrically exact three-dimensional beam theory and its finite-element implementation. *Proceedings of the Royal Society, London: Mathematical, Physical and Engineering Sciences*, 455(1983):1125–1147, 1999.

[43] O.A. Bauchau, A. Epple, and S.D. Heo. Interpolation of finite rotations in flexible multibody dynamics simulations. *Proceedings of the Institution of Mechanical Engineers, Part K: Journal of Multi-body Dynamics*, 222(K4):353–366, 2008.

[44] O.A. Bauchau and S.L. Han. Interpolation of rotation and motion. *Multibody System Dynamics*, 31(3):339–370, 2014.

[45] P. Betsch. The discrete null space method for the energy consistent integration of constrained mechanical systems. Part I: Holonomic constraints. *Computer Methods in Applied Mechanics and Engineering*, 194(50-52):5159–5190, 2005.

[46] P. Betsch and S. Leyendecker. The discrete null space method for the energy consistent integration of constrained mechanical systems. Part II: Multibody dynamics. *International Journal for Numerical Methods in Engineering*, 67:499–552, 2006.

[47] S. Leyendecker, P. Betsch, and P. Steinmann. The discrete null space method for the energy consistent integration of constrained mechanical systems. Part III: Flexible multibody dynamics. *Multibody System Dynamics*, 19(1-2):45–72, 2008.

[48] S.L. Han and O.A. Bauchau. Nonlinear three-dimensional beam theory for flexible multibody dynamics. *Multibody System Dynamics*, 34(3):211–242, July 2015.